# TIME-REVERSAL INDOOR POSITIONING WITH CENTIMETER ACCURACY USING MULTI-ANTENNA WIFI

*Chen Chen*[⋆†], *Yi Han*[⋆†], *Yan Chen*[*†], *Feng Zhang*[⋆†], *and K.J. Ray Liu*[⋆†]

[⋆] University of Maryland, College Park, MD 20742, USA
[†] Origin Wireless, Suite 1070, 7500 Greenway Center Drive, MD 20770, USA
[*] School of Electronic Engineering, University of Electronic Science and Technology of China
Email: {cc8834, yhan1990, fzhang15, kjrliu}@umd.edu[⋆], eecyan@uestc.edu.cn[*]

## ABSTRACT

In this paper, we propose an indoor positioning system (IPS) that achieves centimeter accuracy in a complex indoor environment using time-reversal (TR) technique with a single pair of off-the-shelf multi-antenna WiFi devices. The proposed IPS can work under both line-of-sight (LOS) and non-line-of-sight (NLOS) environment. Leveraging the spatial diversity on the multi-antenna WiFi device, the proposed IPS creates a large effective bandwidth to mitigate the ambiguity between different locations due to the limited bandwidth in WiFi systems. The proposed IPS obtains channel frequency responses (CFRs) from different antenna links at locations-of-interest in the offline phase. In the online phase, it captures instantaneous CFR which is compared against CFRs in the offline phase by fusing the time-reversal resonating strength (TRRS) calculated at each link. Finally, the location is determined according to the TRRS. Extensive experiment results in an office environment demonstrate true positive rates of $99.93\%$ and $100\%$ while only incurring false positive rates of $1.56\%$ and $1.80\%$ under LOS and NLOS conditions, respectively.

***Index Terms***— Time-reversal resonating strength, multi-antenna, channel frequency response, indoor localization.

## 1. INTRODUCTION

Recent years witnesses a rapid growth of the indoor positioning applications, ranging from targeted advertisement in supermarkets [1], shopping mall navigations [2], and personal museum guidance [3]. To enable these applications, a high indoor localization accuracy is required, which cannot be achieved by the Global Positioning System (GPS) mainly due to the severe attenuations and reflections of GPS signals in a complicated indoor environment.

The demand on the high accuracy leads to an extensive development of indoor positioning systems (IPSs) leveraging the radio-frequency (RF) techniques [4]. According to the techniques adopted, these IPSs can be classified into ranging-based and fingerprint-based schemes. For the ranging-based methods, at least three anchors are deployed to triangulate the device by measuring the anchors-to-device distances. The measurement of distance is generally translated from other information. In [5, 6], the received signal strength indicator (RSSI) is utilized to derive the distance with the free-space path loss model to achieve a mean accuracy of $1 \sim 3m$ in line-of-sight (LOS) scenarios. However, the performances of these methods are highly dependent on the correctness of the employed physical model, e.g., the free-space path-loss model. Therefore, the accuracy degrades in a complex indoor environment when the physical model becomes inaccurate.

On the other hand, the fingerprint-based approaches exploit the naturally existing spatial characteristics of different locations, e.g., RSSI, channel impulse response (CIR), and channel frequency response (CFR). In [7–9], RSSI readings from several WiFi access points (APs) are utilized as the fingerprint to achieve an accuracy of $2 \sim 5$m. The accuracy is further enhanced to $0.95 \sim 1.1$m by taking CFRs in WiFi systems as the fingerprint [10–12]. In [13], Wu *et al.* obtain CIR fingerprint under $125$ MHz bandwidth. Then, leveraging the high-resolution spatial-temporal focusing effect of time-reversal (TR) [14], they calculate the TR resonating strength (TRRS) as the similarity metric between fingerprints and thus the associated locations, leading to an accuracy of $1 \sim 2$cm under strong non-line-of-sight (NLOS) settings. Nevertheless, the fingerprint-based approaches using WiFi cannot achieve centimeter accuracy since the limited bandwidth in WiFi networks introduces severe ambiguity among fingerprints at different locations. Meanwhile, specialized hardware with large bandwidth is required in [13] which incurs additional cost in deployment.

To overcome the issue of ambiguity in WiFi-based localization, Chen *et al.* exploit the frequency diversity in WiFi systems by performing frequency hopping to collect CFRs from different frequency bands to achieve centimeter accuracy [15]. However, it might be time-consuming to measure a large number of WiFi channels. Instead of using the frequency diversity, in this paper, we explore the spatial diversity inherent in Multiple-Input-Multiple-Output (MIMO) WiFi systems, which is more time-efficient. The IPS creates a

large effective bandwidth by combining CFRs from different antenna links to improve the performance. The proposed IPS consists of two phases. In the offline phase, the IPS captures CFRs from multiple locations-of-interest. In the online phase, instantaneous CFR is captured and compared against those obtained in the offline phase by evaluating the TRRS. Finally, the IPS determines the locations according to the TRRS.

The rest of the paper is organized as follows. In Section 2, we introduce the signal model of the CFR incorporating synchronization errors. In Section 3, we propose the localization algorithm. The experiment results are illustrated and discussed in Section 4. Finally, Section 5 concludes the paper.

## 2. SIGNAL MODEL

The CFR is a fine-grained frequency-domain information available in OFDM systems that portraits the physical environment. It is a set of channel measurements depicting the amplitudes and phases of each subcarrier in the frequency domain. Specifically, for an MIMO WiFi system, assume a total of $D$ links and $N$ subcarriers, the CFR on the $d$-th link can be written as $\mathbf{H}_d = [H_d[u_1], \cdots, H_d[u_k], \cdots, H_d[u_K]]$, where $H_d[u_k]$ stands for the CFR on the $d$-th link and $k$-th subcarrier with subcarrier index $u_k$. $K$ is the total number of usable subcarriers, which is smaller than $N$ in the presence of null subcarriers.

In practice, the RF front-end of WiFi receiver is not exactly the same as the front-end of the WiFi transmitter, which leads to synchronization errors, including carrier frequency offset (CFO), sampling frequency offset (SFO), and symbol timing offset (STO) [16]. Although WiFi receivers perform timing and frequency synchronization to mitigate the impact of synchronization errors, the residual of them cannot be neglected. The net effect of the synchronization errors is a phase rotation which can be further decomposed into an initial phase rotation and a linear phase rotation. Incorporating the synchronization errors as well as the channel noise, $\hat{\mathbf{H}}_d$ is modified into $\hat{\mathbf{H}}_d = [\hat{H}_d[u_1], \cdots, \hat{H}_d[u_k], \cdots, \hat{H}_d[u_K]]$ takes the form [17]

$$\hat{H}_d[u_k] = H_d[u_k] e^{j(\alpha+\beta u_k)} + W_d[u_k] \,, \tag{1}$$

where $W_d[u_k]$ is the channel noise on the $k$-th subcarrier of link $d$.

## 3. ALGORITHM

In this section, we introduce the algorithm of the proposed IPS with an emphasis on the calculation of TRRS, a metric that evaluates the TR spatial-temporal focusing effect.

### 3.1. Calculating TRRS for Each Link

Given two CIRs $\hat{\mathbf{h}} = [\hat{h}[0], \cdots, \hat{h}[L-1]]$ with $\hat{\mathbf{h}}'$ defined similarly, the TRRS between them is defined in [13], which is given by

$$\gamma[\hat{\mathbf{h}}, \hat{\mathbf{h}}'] = \frac{\max\limits_i \left| \left( \hat{\mathbf{h}} * \hat{\mathbf{g}} \right)[i] \right|^2}{\langle \hat{\mathbf{h}}, \hat{\mathbf{h}} \rangle \langle \hat{\mathbf{g}}, \hat{\mathbf{g}} \rangle} \,, \tag{2}$$

where $*$ stands for the linear convolution, $\hat{\mathbf{g}}$ is the time-reversed and conjugate version of $\hat{\mathbf{h}}'$, and $\langle \mathbf{x}, \mathbf{y} \rangle$ is the inner-product operator between $\mathbf{x}$ and $\mathbf{y}$, calculated by $\mathbf{x}^\dagger \mathbf{y}$, and $(\cdot)^\dagger$ is the Hermitian operator. The denominator of (2) scales $\gamma[\hat{\mathbf{h}}, \hat{\mathbf{h}}']$ into $[0, 1]$. In this regard, TRRS essentially measures the similarity between two CIRs.

Realizing that convolution in the time domain can be reformulated as the inner-product in the frequency domain, TRRS can be calculated using frequency domain CFRs directly. Assuming two CFRs on link $d$ given by $\hat{\mathbf{H}}_d$ and $\hat{\mathbf{H}}'_d$, the TRRS can be written as

$$\gamma[\hat{\mathbf{H}}_d, \hat{\mathbf{H}}'_d] = \frac{\phi_d}{\Lambda_d \Lambda'_d} \,, \tag{3}$$

where $\phi_d = \max\limits_{\epsilon} \left| \sum_{k=1}^{K} \hat{H}_d[u_k] \hat{H}'_d[u_k] e^{-j\epsilon u_k} \right|^2$, $\Lambda_d = \langle \hat{\mathbf{H}}_d, \hat{\mathbf{H}}_d \rangle$, and $\Lambda'_d = \langle \hat{\mathbf{H}}'_d, \hat{\mathbf{H}}'_d \rangle$. The linear phase distortion is compensated in $\phi_d$ by maximizing over $\epsilon$, and the initial phase distortion is mitigated by taking absolute value in calculating $\phi_d$.

An exhaustive search over $\epsilon \in [-\pi, +\pi]$ leads to the optimum precision in evaluating $\phi_d$, but incurs heavy computational burden. To calculate $\phi_d$ efficiently and accurately with an effective search resolution of $2\pi/N'$, we approximate $\phi_d$ with $\overline{\phi}_d$ given by

$$\overline{\phi}_d = \max_n \Bigg| \underbrace{\sum_{k=1}^{K} \hat{H}_d[u_k] \hat{H}'_d[u_k] e^{-j\frac{2\pi n}{N'} u_k}}_{z[n]} \Bigg|^2 . \tag{4}$$

Realizing that $z[n]$ shares the same form of an $N'$-point discrete Fourier transform (DFT), we employ the fast Fourier transform (FFT) to accelerate the calculation. When $N'$ is large, $\phi_d \approx \overline{\phi}_d$, and $\gamma[\hat{\mathbf{H}}_d, \hat{\mathbf{H}}'_d]$ can be well approximated by $\overline{\phi}_d / (\Lambda_d \Lambda'_d)$.

### 3.2. Calculating Combined TRRS

After calculating $\overline{\phi}_d$ from CFR measurements of all $D$ links, denoted by $\hat{\mathbb{H}} = [\hat{\mathbf{H}}_1, \cdots, \hat{\mathbf{H}}_D]$ and $\hat{\mathbb{H}}' = [\hat{\mathbf{H}}'_1, \cdots, \hat{\mathbf{H}}'_D]$, the IPS fuses the TRRS at different links into the *combined TRRS* denoted by $\gamma[\hat{\mathbb{H}}, \hat{\mathbb{H}}']$ shown as

$$\gamma[\hat{\mathbb{H}}, \hat{\mathbb{H}}'] = \left( \frac{\sum_{d=1}^{D} \sqrt{\Lambda_d \Lambda'_d \gamma[\hat{\mathbf{H}}_d, \hat{\mathbf{H}}'_d]}}{\sqrt{\sum_{d=1}^{D} \Lambda_d} \sqrt{\sum_{d=1}^{D} \Lambda'_d}} \right)^2 . \tag{5}$$

Since we fully utilize the information in $\hat{\mathbb{H}}$ and $\hat{\mathbb{H}}'$ in calculating $\gamma[\hat{\mathbb{H}}, \hat{\mathbb{H}}']$, we achieve an effective bandwidth $W_e = DKB/N$, where $B$ is the bandwidth per link.

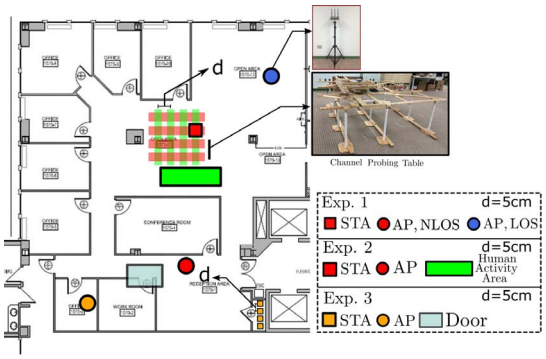


**Fig. 1**: Experiment settings.

| | $W_e$ (MHz) | 36 | 143 | 249 | 321 |
|---|---|---|---|---|---|
| Exp. 1 NLOS | $\Gamma$ | 0.78 | 0.60 | 0.55 | 0.54 |
| | $\mathbb{P}_{\mathsf{TP}}(\%)$ | 100 | 100 | 100 | 100 |
| | $\mathbb{P}_{\mathsf{FP}}(\%)$ | 1.73 | 1.82 | 1.56 | 1.80 |
| Exp. 1 LOS | $\Gamma$ | 0.86 | 0.71 | 0.65 | 0.64 |
| | $\mathbb{P}_{\mathsf{TP}}(\%)$ | 100 | 99.91 | 99.91 | 99.93 |
| | $\mathbb{P}_{\mathsf{FP}}(\%)$ | 1.98 | 1.67 | 1.93 | 1.56 |
| Exp. 2 Human Activities | $\Gamma$ | 0.84 | 0.62 | 0.56 | 0.53 |
| | $\mathbb{P}_{\mathsf{TP}}(\%)$ | 97.94 | 99.94 | 99.94 | 99.89 |
| | $\mathbb{P}_{\mathsf{FP}}(\%)$ | 1.72 | 1.97 | 1.64 | 1.94 |
| Exp. 3 Large Object | $\Gamma$ | – | – | 0.54 | 0.51 |
| | $\mathbb{P}_{\mathsf{TP}}(\%)$ | – | – | 92 | 98.37 |
| | $\mathbb{P}_{\mathsf{FP}}(\%)$ | – | – | 1.62 | 1.70 |

**Table 1**: Settings of $\Gamma$ to achieve $\mathbb{P}_{\mathsf{TP}} \geq 90\%$ and $\mathbb{P}_{\mathsf{FP}} \leq 2\%$.

### 3.3. Localization Using Combined TRRS

The localization in the proposed IPS consists of an offline phase and an online phase. We elaborate on the two phases in the subsequent parts of this section.

#### *3.3.1. Offline Phase*

In this phase, we collect $R$ snapshots of CFRs from each of the $L$ locations-of-interest. The $L \times R$ CFRs are stored into the training database $\mathbb{D}_{\mathsf{train}}$, where the $i$-th row of $\mathbb{D}_{\mathsf{train}}$ is the CFR vector $\hat{\mathbb{H}}_i$ shown in Section 3.2, and $i$ is the *training index*. Denote the snapshot index as $r$ and the location index as $\ell$, the training index $i$ can be mapped from $(r, \ell)$ as $i = (\ell - 1)R + r$.

#### *3.3.2. Online Phase*

In this phase, assume that we collect the instantaneous CFR $\hat{\mathbb{H}}'$ at an unknown location $\ell'$. To estimate $\ell'$, we first calculate the TRRS between each CFR in $\mathbb{D}_{\mathsf{train}}$ and $\hat{\mathbb{H}}'$ which leads to $\{\gamma[\hat{\mathbb{H}}_i, \hat{\mathbb{H}}']\}_{i \in \mathcal{L}}$, where $\mathcal{L} = \{0, 1, 2, \cdots, L\}$ is the location candidate. The location index 0, termed as the *unmapped location*, is also included into $\mathcal{L}$ since it is possible that the instantaneous CFR is obtained at an unmapped position.

Based on $\{\gamma[\hat{\mathbb{H}}_i, \hat{\mathbb{H}}']\}_{i \in \mathcal{L}}$, we search for the training index $i$ that best matches the instantaneous CFR. The estimated training index $\widehat{i}$ can be written as

$$\widehat{i} = \begin{cases} \underset{i=1,2,\cdots,L}{\arg\max}\, \gamma[\hat{\mathbb{H}}_i, \hat{\mathbb{H}}'], & \underset{i=1,2,\cdots,L}{\max}\, \gamma[\hat{\mathbb{H}}_i, \hat{\mathbb{H}}'] \geq \Gamma \\ 0, & \text{Otherwise}, \end{cases} \tag{6}$$

where $\Gamma$ is the threshold. Finally, the estimated location index $\hat{\ell}'$ is mapped back from $\widehat{i}$ by

$$\hat{\ell}' = \begin{cases} \mathrm{mod}(\widehat{i} - 1, R) + 1, & \widehat{i} \neq 0 \\ 0, & \text{Otherwise}, \end{cases} \tag{7}$$

where $\mathrm{mod}(x, y)$ is the modulus operator on $x$ with base $y$.

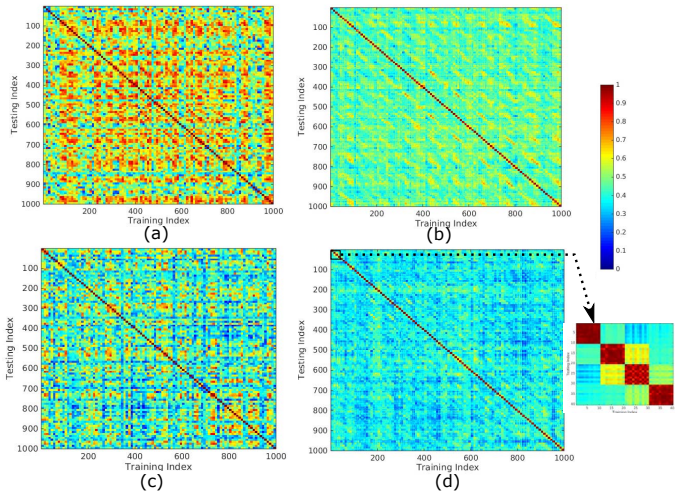


**Fig. 2**: Results of Exp. 1 under (a) LOS, $W_e = 36$ MHz (b) LOS, $W_e = 321$ MHz. (c) NLOS, $W_e = 36$ MHz (d) NLOS, $W_e = 321$ MHz.

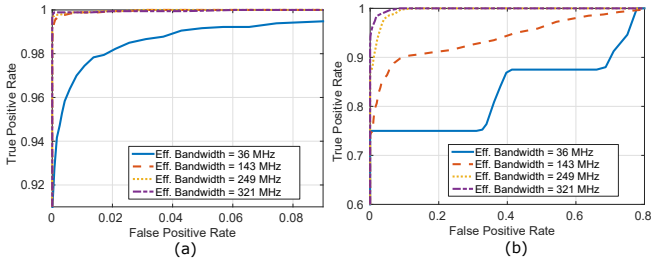


**Fig. 3**: ROC curves under different $W_e$. (a) Exp. 2 with human activities (b) Exp. 3 with large object movement.

## 4. EXPERIMENT RESULTS

### 4.1. Experiment Settings

The experiments are conducted in a typical office in a multi-storey building. The office is occupied by desks, computers, chairs, and shelves. We use one pair of off-the-shelf WiFi devices with modified driver to facilitate CSI acquisition. Each WiFi device is equipped with 3 omnidirectional antennas. Therefore, the total number of links $D$ is 9. One of the WiFi devices acts as an AP, and the other works as a station (STA).

We conduct three experiments using the settings in Fig. 1 with details given below: (i) **Exp.** 1 is targeted to verify the centimeter accuracy of the proposed IPS. The AP is placed at two different positions to evaluate the performances under strong LOS and strong NLOS scenarios, respectively, while the STA is placed on a measurement platform with 5 cm resolution. For each AP position, CFRs at a total of $L = 100$ locations on the platform are collected, with $R = 10$ CFRs per location. (ii) **Exp.** 2 is used to evaluate the IPS performance in the presence of human activities. One participant is asked to walk randomly in close vicinity to the STA. CFRs from $L = 40$ different locations on the measurement platform with 5 cm resolution are obtained, with $R = 10$ CFRs per location. (iii) **Exp.** 3 is conducted to assess the IPS performance with dynamics from large object movement. The AP is placed in a small room, while the STA is placed at $L = 4$ positions with 5 cm resolution in a closet. One participant operates a door at the middle of the direct link between AP and STA. CFRs from 4 positions in the closet are captured with 10 CFRs for each location.

The effective bandwidth $W_e$ in the experiments is calculated using $DKB/N$ as shown in Section 3, with $K = 114$, $N = 128, B = 40$MHz, and $D = 1, 2, 3, \cdots, 9$. $N'$ is configured as 1024.

For the purpose of performance evaluation, we store all CFRs into $\mathbb{D}_{\mathsf{train}}$ and make the testing database $\mathbb{D}_{\mathsf{test}}$ to be the same as $\mathbb{D}_{\mathsf{train}}$. Essentially, we are assessing the similarity among the same locations and dissimilarity among different locations. Then, using CFRs in $\mathbb{D}_{\mathsf{train}}$ and $\mathbb{D}_{\mathsf{test}}$, we calculate the TRRS matrix $\mathbb{R}$ with its $(i, j)$-th entry as $\gamma[\hat{\mathbb{H}}_i, \hat{\mathbb{H}}_j]$, where $\hat{\mathbb{H}}_i$ is the $i$-th row of $\mathbb{D}_{\mathsf{train}}$ and $\hat{\mathbb{H}}_j$ is the $j$-th row of $\mathbb{D}_{\mathsf{test}}$. $j$ is denoted as the *testing index*.

Based on $\mathbb{R}$, we evaluate the localization performances by the **true positive rate**, denoted as $\mathbb{P}_{\mathsf{TP}}$, and the **false positive rate**, denoted as $\mathbb{P}_{\mathsf{FP}}$. $\mathbb{P}_{\mathsf{TP}}$ is defined as the probability that the AP localizes the STA to the correct locations, while $\mathbb{P}_{\mathsf{FP}}$ is defined as probability that the AP localizes the STA to the incorrect locations or the unmapped location. We also show the Receiver Operating Characteristic (ROC) curves to highlight the trade-off between $\mathbb{P}_{\mathsf{TP}}$ and $\mathbb{P}_{\mathsf{FP}}$.

### 4.2. Performance Evaluation

In Fig. 2, we show the TRRS matrix $\mathbb{R}$ under different $W_e$ in both NLOS and LOS scenarios. As can be seen from Fig. 2, increasing $W_e$ reduces the TRRS among different locations, as can be observed from the decreasing off-diagonal part in $\mathbb{R}$. Therefore, a large $W_e$ mitigates the ambiguities among different locations. Additionally, we illustrate the details of the diagonal part of $\mathbb{R}$ in Fig. 2(d) when $W_e = 321$ MHz, which shows that TRRS calculated at the same location is close to 1, indicating high similarity. Comparing Fig. 2(a),(b) with Fig. 2(c),(d), we find that the location distinction is less pronounced under the LOS case, since there exist only a few significant multipath components and reduces the distinction between locations consequently.

In Table 1, we show the smallest $\Gamma$ that could achieve $\mathbb{P}_{\mathsf{TP}} \geq 90\%$ with $\mathbb{P}_{\mathsf{FP}} \leq 2\%$. We observe that $\Gamma$ decreases when $W_e$ increases. When $W_e = 321$ MHz, $\mathbb{P}_{\mathsf{TP}}$ reach $100\%$ and $99.93\%$ while $\mathbb{P}_{\mathsf{FP}}$ are merely $1.80\%$ and $1.56\%$ for the NLOS and LOS scenarios, respectively.

Fig. 3(a) illustrates the ROC curve using different $W_e$ under the influence of human activities. The results indicate that a large $W_e$ can enhance the robustness of localization. As shown in Table 1, when $W_e = 321$ MHz, a threshold of $0.53$ suffices to make $\mathbb{P}_{\mathsf{TP}} = 99.89\%$ and $\mathbb{P}_{\mathsf{FP}} = 1.74\%$.

The impact of large object movement on localization is more severe than the human activities. In Fig. 3(b), we illustrate the results with a door opening/closing using different $W_e$. In this case, a large $W_e$ is indispensable. According to Table 1, when $W_e \leq 249$ MHz, we fail to find a $\Gamma$ that makes $\mathbb{P}_{\mathsf{TP}} \geq 90\%, \mathbb{P}_{\mathsf{FP}} \leq 2\%$. The performance improves dramatically with $W_e = 321$ MHz, which boosts $\mathbb{P}_{\mathsf{TP}}$ to $98.37\%$ with $\mathbb{P}_{\mathsf{FP}}$ at $1.70\%$.

From the experiment results above, we conclude that the proposed IPS achieves centimeter localization accuracy with very high true positive rates and negligible false positive rates. In fact, our recent results with $0.5$ cm measurement resolution show a promising $1-2$ cm localization accuracy in an NLOS environment, which is not shown here due to the page limit.

## 5. CONCLUSION

In this paper, we propose an IPS embracing the time-reversal focusing effect for centimeter accuracy indoor localization on commercial WiFi devices. The proposed IPS harvests the spatial diversity in MIMO WiFi systems to formulate a large effective bandwidth. Extensive experimental results show that the proposed IPS achieves centimeter accuracy with true positive rates of $99.93\%$ and $100\%$, and incurs false positive rates of $1.56\%$ and $1.80\%$ under the LOS and NLOS scenarios, respectively. Meanwhile, the IPS is robust against the environment dynamics caused by human activities and object movements.

## 6. REFERENCES


[1] K.-L. Sue, "Mambo: A mobile advertisement mechanism based on obscure customer's location by RFID," in *Computing, Measurement, Control and Sensor Network (CMCSN), 2012 International Conference on*, pp. 425–428, July 2012.

[2] L. Wang, W. Liu, N. Jing, and X. Mao, "Simultaneous navigation and pathway mapping with participating sensing," *Wirel. Netw.*, vol. 21, pp. 2727–2745, Nov. 2015.

[3] E. Bruns, B. Brombach, T. Zeidler, and O. Bimber, "Enabling mobile phones to support large-scale museum guidance," *IEEE MultiMedia*, vol. 14, pp. 16–25, April 2007.

[4] H. Liu, H. Darabi, P. Banerjee, and J. Liu, "Survey of wireless indoor positioning techniques and systems," *IEEE Trans. Syst., Man, Cybern., Syst.*, vol. 37, pp. 1067–1080, Nov 2007.

[5] J. Hightower, R. Want, and G. Borriello, "SpotON: An indoor 3D location sensing technology based on RF signal strength," UW CSE 00-02-02, University of Washington, Department of Computer Science and Engineering, Seattle, WA, February 2000.

[6] L. Ni, Y. Liu, Y. C. Lau, and A. Patil, "LANDMARC: indoor location sensing using active RFID," in *Pervasive Computing and Communications, 2003. (PerCom 2003). Proceedings of the First IEEE International Conference on*, pp. 407–415, March 2003.

[7] P. Bahl and V. Padmanabhan, "RADAR: an in-building RF-based user location and tracking system," in *Proc. IEEE INFOCOM*, vol. 2, pp. 775–784 vol.2, 2000.

[8] M. Youssef and A. Agrawala, "The Horus WLAN location determination system," in *Proceedings of the 3rd International Conference on Mobile Systems, Applications, and Services*, MobiSys '05, (New York, NY, USA), pp. 205–218, ACM, 2005.

[9] P. Prasithsangaree, P. Krishnamurthy, and P. Chrysanthis, "On indoor position location with wireless LANs," in *Personal, Indoor and Mobile Radio Communications, 2002. The 13th IEEE International Symposium on*, vol. 2, pp. 720–724 vol.2, Sept 2002.

[10] S. Sen, B. Radunovic, R. R. Choudhury, and T. Minka, "You are facing the Mona Lisa: Spot localization using PHY layer information," in *Proceedings of the 10th International Conference on Mobile Systems, Applications, and Services*, MobiSys '12, (New York, NY, USA), pp. 183–196, ACM, 2012.

[11] J. Xiao, W. K.S., Y. Yi, and L. Ni, "FIFS: Fine-grained indoor fingerprinting system," in *Computer Communications and Networks (ICCCN), 2012 21st International Conference on*, pp. 1–7, July 2012.

[12] Y. Chapre, A. Ignjatovic, A. Seneviratne, and S. Jha, "CSI-MIMO: Indoor Wi-Fi fingerprinting system," in *Local Computer Networks (LCN), 2014 IEEE 39th Conference on*, pp. 202–209, Sept 2014.

[13] Z.-H. Wu, Y. Han, Y. Chen, and K. J. R. Liu, "A time-reversal paradigm for indoor positioning system," *IEEE Trans. Veh. Commun.*, vol. 64, pp. 1331–1339, April 2015.

[14] B. Wang, Y. Wu, F. Han, Y.-H. Yang, and K. J. R. Liu, "Green wireless communications: A time-reversal paradigm," *IEEE J. Select. Areas Commun.*, vol. 29, pp. 1698–1710, September 2011.

[15] C. Chen, Y. Chen, L. Hung-Quoc, Y. Han, and K. J. R. Liu, "High accuracy indoor localization: A WiFi-based approach," in *Proc. IEEE International Conference on Acoustics, Speech and Signal Processing (ICASSP)*, March 2016.

[16] T.-D. Chiueh and P.-Y. Tsai, *OFDM Baseband Receiver Design for Wireless Communications*. John Wiley and Sons (Asia) Pte Ltd, 2007.

[17] M. Speth, S. Fechtel, G. Fock, and H. Meyr, "Optimum receiver design for wireless broad-band systems using OFDM—Part I," *IEEE Trans. Commun.*, vol. 47, pp. 1668–1677, Nov 1999.